ADVANCED MATERIALS
www.advmat.de

Shape Morphing Directed by Spatially Encoded, Dually Responsive Liquid Crystalline Elastomer Micro-Actuators

*Mingzhu Liu, Lishuai Jin, Shengsong Yang, Yuchen Wang, Christopher B. Murray, and Shu Yang**

Liquid crystalline elastomers (LCEs) with intrinsic molecular anisotropy can be programmed to morph shapes under external stimuli. However, it is difficult to program the position and orientation of individual mesogenic units separately and locally, whether in-plane or out-of-plane, since each mesogen is linked to adjacent ones through the covalently bonded polymer chains. Here, dually responsive, spindle-shaped micro-actuators are synthesized from LCE composites, which can reorient under a magnetic field and change the shape upon heating. When the discrete micro-actuators are embedded in a conventional and nonresponsive elastomer with programmed height distribution and in-plane orientation in local regions, robust and complex shape morphing induced by the cooperative actuations of the locally distributed micro-actuators, which corroborates with finite element analysis, are shown. The spatial encoding of discrete micro-actuators in a nonresponsive matrix allows to decouple the actuators and the matrix, broadening the material palette to program local and global responses to stimuli for applications including soft robotics, smart wearables, and sensors.

1. Introduction

Liquid crystalline elastomers (LCEs) with pre-aligned liquid crystal mesogens (the building blocks) in the network offer programmable large and reversible deformation upon stimulation.[1] Therefore, they are promising for applications, including shape transformation,[2] actuators,[3–5] artificial cilia,[6,7] artificial muscles,[8] and soft robotics.[9–14] As the mesogens undergo phase transition from nematic (the aligned state) to isotropic state, the polymer network shrinks along the alignment axis accompanied by expansion in the direction perpendicular to the alignment. Thus, the complexity and diversity of shape transformations are highly dependent on the spatial orientation (or the director field) of the LC mesogens.[15–21] A variety of methods[22] have been developed to control the in-plane director field, including mechanically stretching/shearing,[23–25] guiding by surface patterns,[16,26–28] and use of electric or magnetic field.[29] Out-of-plane bending of a flat LCE film can be realized when there is a gradient in the director field induced by different surface anchoring on top and bottom of the film[30,31] or in mechanical properties along the film thickness.[32–34] So far few have shown control of both in-plane and out-of-plane orientations of LC mesogens with complex director fields in the 3D space, locally and globally. Using a top and bottom substrate with planar microchannels oriented in different directions has shown such potentials.[28] However, the thickness of films (up to 100 μm) is limited by the decreasing molecular interactions away from the surface, causing deviation of the mesogens from the aligned direction along film depth. 3D printing allows for arbitrary arrangement of mesogens in 3D space, however, the printing resolution is typically on the order of hundreds of micrometers to millimeters. Thus, only simple geometries are printed, and it is time consuming to build layer-by-layer. While the intrinsic anisotropy of LC mesogens enables reversible actuation, it also constrains the choice of materials, fabrication, and spatial control of the shape morphing, due to the coupling between these aspects.

Incorporating LCEs with other materials provides a feasible pathway to expand the materials library for shape morphing. A bilayer-structure of LCE and hydrogel with different elasticity has been demonstrated.[35,36] However, a strong bonding between the two layers is essential, otherwise, it will lead to a small strain[35] and poor reversibility.[36] Microparticles made by freeze-milling the bulk LCE film have been embedded in a conventional elastomer, polydimethylsiloxane (PDMS), followed by alignment under an external magnetic field to create macroscopic "monodomains" for actuation.[37] The use of discrete microparticles allows for decoupling of the enabling components[38] from the matrix itself. Nevertheless, those microparticles are not uniform in size nor anisotropic in shape. They are only aligned along an in-plane direction and a bilayer structure is still needed to achieve out-of-plane bending. Furthermore, the magnetic field-induced mesogen alignment is mostly limited to side-chain LC monomers due to high viscosity of main-chain system. Main-chain LCE microparticles[39–44] (Young's modulus E, ≈ 10's MPa) or side-chain LCE micro-actuators[45,46]

M. Liu, L. Jin, Y. Wang, C. B. Murray, S. Yang
Department of Materials Science and Engineering
University of Pennsylvania
Philadelphia, PA 19104, USA
E-mail: shuyang@seas.upenn.edu
S. Yang, C. B. Murray
Department of Chemistry
University of Pennsylvania
Philadelphia, PA 19104, USA
The ORCID identification number(s) for the author(s) of this article can be found under https://doi.org/10.1002/adma.202208613.

DOI: 10.1002/adma.202208613

with well-defined shapes and thermal responsiveness have been synthesized to study the shape changes of the particles themselves. They are yet to be embedded in a polymer matrix for study of programmable shape morphing due to lack of controlled in-plane orientation and thickness-wise distribution. Often the particles are not uniform in size, thus their response to external stimuli may not be uniform.

Here, we design and synthesize dually responsive, spindle-shaped, and uniform-sized micro-actuators from main-chain LCE composites consisting of magnetic nanoparticles. The micro-actuators can be aligned in-plane using a magnetic field and embedded into poly(ethylene glycol) diacrylate (PEGDA), an isotropic elastomer that is softer than LCE, to direct the actuation (via bending). The arrangement of micro-actuators can be controlled by three strategies: 1) Using gravity to direct height distribution of the LCE micro-actuators within the film, 2) photopatterning monodomains of LCE micro-actuators to program the in-plane director fields in a stepwise fashion, and 3) programming the in-plane director field of the LCE micro-actuators in a single step using a 2D magnetic field. Combining these strategies enables simultaneous programming of the out-of-plane and in-plane directions of bending spatially, leading to complex shape morphing, including switching the bending directions, forming of a negative Gaussian curvature, opening of four distinct "pedals," generating of a "crawler," and morphing of a bumpy surface. The targeted actuation behaviors corroborate with simulation, supporting the robustness of our strategies.

2. Results and Discussion

2.1. Design and Synthesis of Dually Responsive Micro-Actuators

The spindle-shaped micro-actuators are synthesized from microdroplets consisting of LCE precursors dispersed with paramagnetic nanoparticles[47] ($Mn_{0.4}Zn_{0.6}Fe_2O_3$ nanoparticles, MZF NPs, Figure S1, Supporting Information), followed by photopolymerization. The LCE precursor consists of reactive mesogenic monomer, 1,4-bis-[4-(6-acryloyloxy-hexyloxy) benzoyloxy]-2-methylbenzene (RM82), thiol-terminated oligomer, 1,4-bis-[4-(3-acryloyloxy-proplyoxy)benzoyloxy]-2-methylbenzene-1,3-propanedithiol (RM257-1,3 PDT), synthesized according to literature,[48] and small molecule LC, 4′-pentyl-4-biphenylcarbonitrile (5CB), to enhance surface anchoring of mesogens at the interface (Figure S2, Supporting Information). We can vary RM82 to RM257-1,3 PDT molar ratios to tune the nematic-to-isotropic phase transition temperature (T_{NI}) of the precursors according to literature.[48]

Droplets of precursors, photoinitiator, and MZF NPs dispersed in dichloromethane (DCM) are produced with a flow-focusing microfluidic device and suspended in a mixed solution of water/glycerol/poly(vinyl alcohol) (PVA). At this stage, the droplets are in the isotropic phase. After DCM is evaporated at 50 °C, LC molecules in the nematic phase are aligned into a bipolar configuration, where PVA acts as the planar anchoring surfactant. The droplets are then photopolymerized, forming a twisted bipolar director field within the microparticles, while remains to be spherical due to anisotropic elastic constants within the particle.[42,49] Since 5CB is nonreactive, it is removed by ethanol.[42,49] The increased elasticity and amplified anisotropy within the particle lead to the formation of the spindles with uniform size and shape (Figure S3, Supporting Information): the microsphere shrinks in the direction transverse to the director field without noticeable size change along the director field. The spindle microparticles, which we now refer as micro-actuators, have length ($L \approx 45$ μm) and diameter at the equatorial plane ($D \approx 30$ μm) measured from scanning electron microscopy (SEM) (Figure S2c, Supporting Information).

In this study, the micro-actuators are made from oligomer to monomer with molar ratio of 1.4 with $T_{NI} \approx 132$ °C, measured by differential scanning calorimetry (DSC) (Figure S4, Supporting Information). Upon heating from 25 to 175 °C, the long axis of the micro-actuator contracts while the equatorial plane expands, in concert with the continuous shape transition from spindle to spherical (≈ 140 °C, ≈ 16% shrinkage along length and ≈ 14% expansion along width), then to lens-like (≈ 175 °C, ≈30% shrinkage along length and ≈ 27% expansion along width compared to the original shape) (**Figure 1**a). The original spindle shape is recovered after cooling back to 25 °C.

The incorporation of paramagnetic MZF NPs makes the micro-actuators responsive to the magnetic field (Movie S1, Supporting Information) but not retaining any permanent magnetism to cause the transportation of micro-actuators under the field; the anisotropic spindle shape makes them orient preferably in the direction perpendicular to the external field.[50] When the micro-actuators are suspended in a medium with a lower density, the gravitational force drives them to the bottom of the suspension. Applying an in-plane uniform magnetic field can induce the reorientation of micro-actuators, forming a monodomain of micro-actuators (Figure 1b). COMSOL calculation confirms the uniformity of the magnetic field formed between two parallel magnets (Figure S5c, Supporting Information). Since the responsiveness to temperature and magnetic field are orthogonal to each other, it offers a design space to spatially encode the alignment of micro-actuators and their reshaping behaviors to generate complex actuation ensembles.

2.2. Alignment of Micro-Actuators in a Conventional Elastomer to Direct Bending of the Film

The shape change of the aligned micro-actuators drives the bending toward where the micro-actuators are situated within the soft elastomer matrix, PEGDA crosslinked with 2,2′-(ethylenedioxy)diethanethiol (EDDT) and pentaerythritol tetrakis(3-mercaptopropionate) (PETMP), similar to that of a bi-layer structure (**Figure 2**a and Figure S6, Supporting Information). The degree of bending is highly dependent on the uniformity of the alignment of the micro-actuators in the film. PEGDA elastomer is chosen because it is thermally stable in the working temperature range of the micro-actuators, its mechanical properties can be fine-tuned by adjusting the ratio of precursors, and the similar thiol-acrylate chemistry to crosslink PEGDA elastomer and LCE micro-actuators offers good adhesion between them. Here Young's modulus of the PEGDA, $E \approx 0.35 \pm 0.04$ MPa (Figure S7a, Supporting

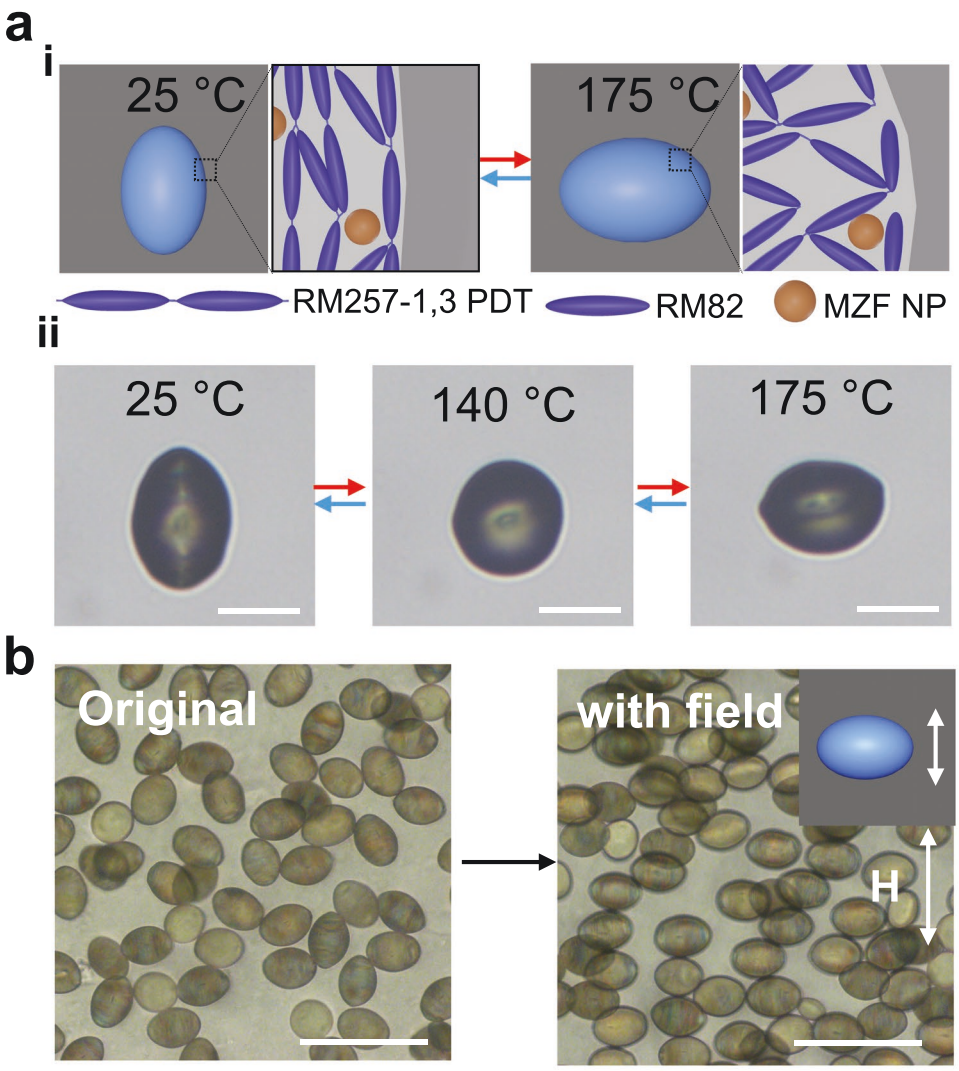

Figure 1. Dually responsive micro-actuators. a) (i) Schematic illustration and (ii) bright-field optical microscopy images of a representative micro-actuator at different temperatures. The shape reversibly changes from spindle (25 °C) to sphere (140 °C), then to lens-like (175 °C) along with the phase transition of LCEs network. b) Bright-field optical microscopy images of the micro-actuators dispersed in the precursors of PEGDA before (left) and after (right) applying a uniform magnetic field. Scale bars: 30 µm for (a), and 100 µm for (b).

Information), is much smaller than that of LCE micro-actuator ($E \approx 15.8 \pm 2.7$ MPa, Figure S7b, Supporting Information). The latter are first dispersed in PEGDA precursor and aligned near the bottom of the film by applying a uniform magnetic field before PEGDA is cured (Figure S5, Supporting Information). The composite elastomer film is slightly stiffer ($E \approx 0.39 \pm 0.14$ MPa) along the alignment direction than the pristine film.

When the micro-actuators are heated, the size in the aligned direction is dramatically reduced (Figure 2a(i,iii)), causing the PEGDA film to bend toward the side with micro-actuators (Figure 2a(ii,iii)). To validate our hypothesis for design of more sophisticated director fields, we use finite element analysis (FEA) to simulate the bending using the parameters obtained by fitting experimental results. For simplification, the discrete micro-actuators are treated as a continuous active layer with thickness of 30 µm and the PEGDA elastomer as a passive layer (Figure 2a(iv)). The edge-to-edge distance along the in-plane direction of bending is measured to characterize the degree of bending of the elastomer film (1 cm × 1 cm), which can be tuned by the concentration of micro-actuators (as weight in mg over the volume of the precursors in µL, w/v), the thickness of PEGDA film, and temperature (Figure 2b,c; Figures S8 and S9, Supporting Information). Higher concentration, smaller thickness, or higher temperature generates more bending. We keep the concentration of micro-actuators in the PEGDA precursor at 15% w/v and the film thickness at 200 µm for the studies reported below. When heated to 180 °C, ≈ 16% shrinkage (estimated by the distance change of two points in Figure 2a(i)) is obtained along the alignment direction of the micro-actuators. The heating (180 °C, to bend) and cooling (25 °C, to recover) cycle (Figure 2d and Figure S10, Supporting Information) is repeated 20 times without noticeable degradation or fatigue.

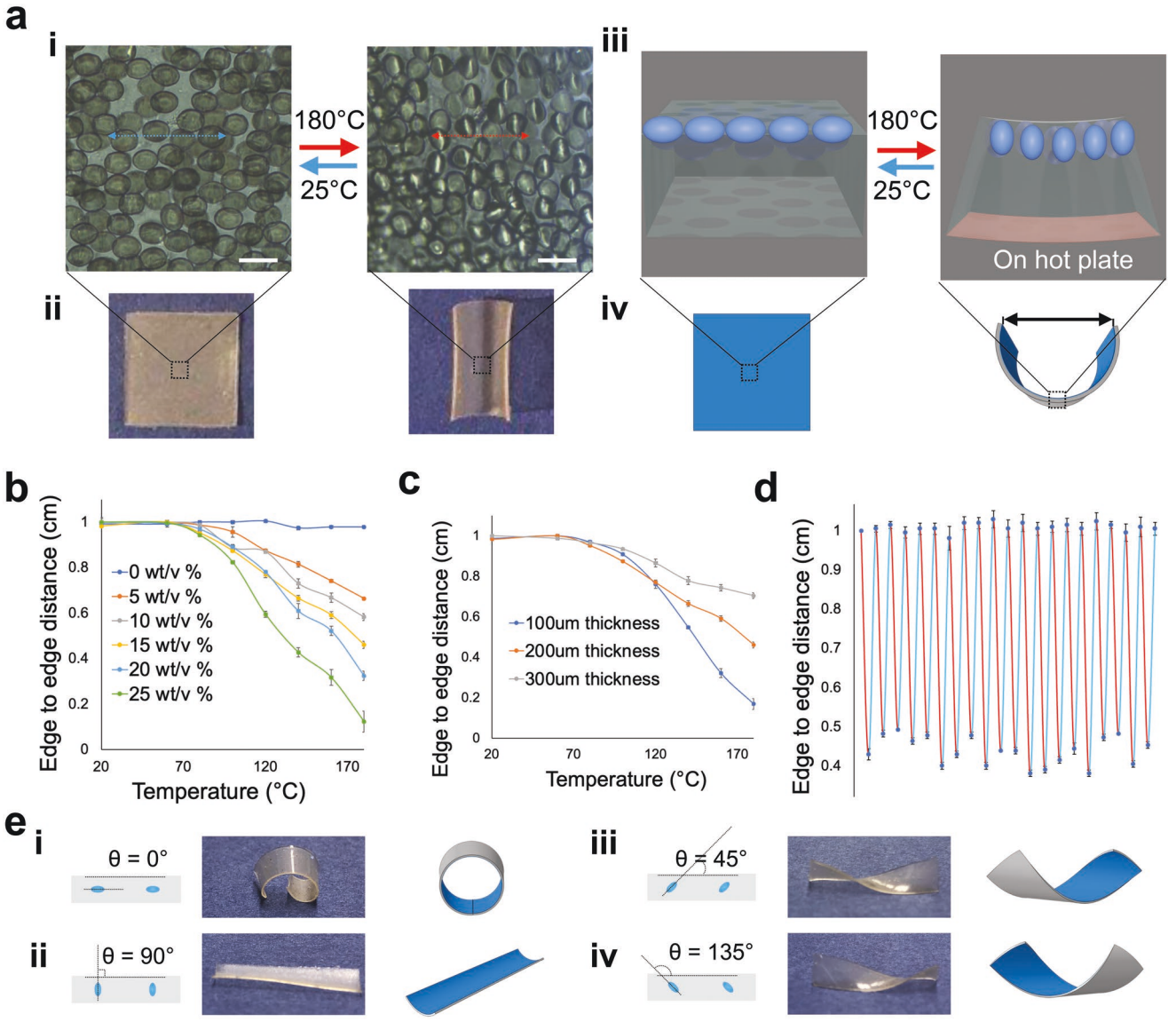

Figure 2. Bending of PEGDA elastomer films embedded with aligned micro-actuators. a) (i) Bright-field microscopy images. The double arrow indicates the preferred initial orientation of the long axial of micro-actuators. (ii) Photos of the composite film before and after heating. (iii) Schematic illustrations of the orientation of the micro-actuators in PEDGA film. (iv) FEA simulation of the composite film before and after heating. The black double arrow indicates edge-to-edge distance of a film. b,c) The edge-to-edge distance as a function of temperature for films with different concentrations of the micro-actuators (b) and film thickness (c). d) Cycling of the bending and flattening of the PEGDA film (thickness, 200 µm) embedded with 15 w/v% micro-actuators between heating to 180 °C on a hot plate (red line) and cooling down to room temperature (≈ 25 °C, blue line) 20 times. Error bars in (b–d) represent the standard deviation of three averaged measurements of randomly picked positions. e) Programmed actuation of the strips embedded with micro-actuators oriented in a certain angle, θ, relative to the long axis of the rectangular strips: illustration (left), observed bending behaviors on a 180 °C hot plate (middle), and the corresponding FEA simulation (right). The angles are 0° (i), 90° (ii), 45° (iii), and 135° (iv). Sample sizes: 1 cm × 1 cm × 200 µm for (a–d), and 2 cm × 0.5 cm × 200 µm for (e). Scale bars: 50 µm.

We then investigate control of the angle (θ) between the alignment direction of the micro-actuators and the geometric long axis of the rectangular PEGDA film (Figure 2e). When the director field is parallel to the long axis ($\theta = 0^{o}$), the film bend into a closed loop (Figure 2e(i)). At $\theta = 90^{o}$, the film bends along the short axis (Figure 2e(ii)). At $\theta = 45^{o}$ or 135^{o}, helical structures are generated (Figure 2e(iii,iv)), consistent with FEA simulation. Therefore, we can customize the alignment of the micro-actuators to direct the bending direction of the composite film, akin to programming the alignment of the molecular mesogens in pure LCE films,[15,19,51] except that here LCE micro-actuators are not crosslinked in the PEGDA network.

2.3. Programmed Bending of the PEGDA Films

Next, we exploit three different strategies to program the bending behaviors. First, we spatially control the height distribution of the micro-actuators in the PEGDA film (**Figure 3**a). After the micro-actuators sink to the bottom of the precursor

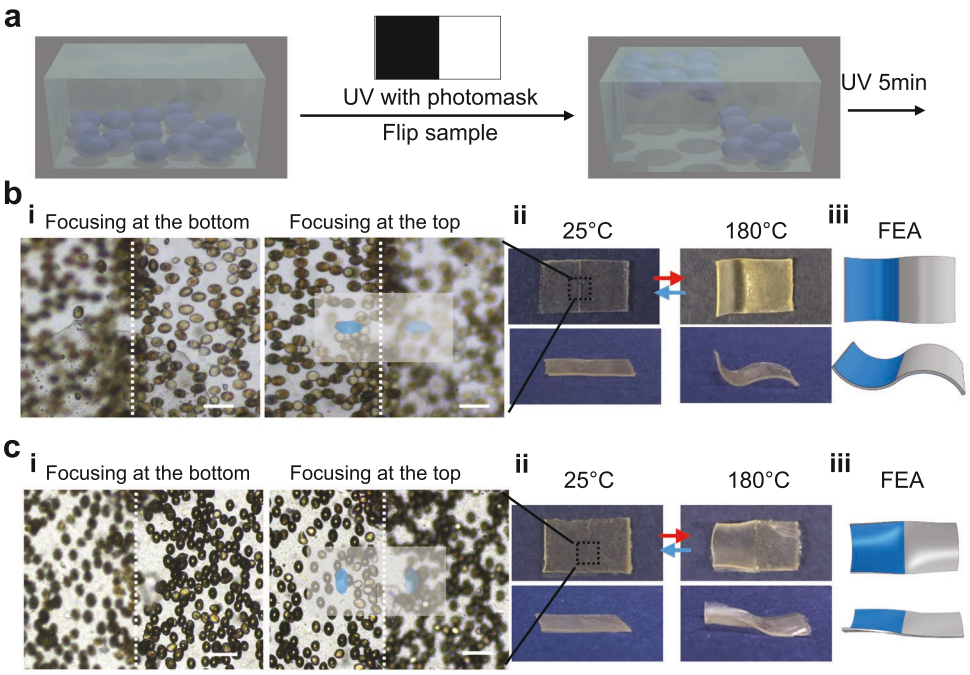

Figure 3. Programmed out-of-plane bending. a) Schematic illustration of controlling the height distribution of the aligned micro-actuators within PEGDA film under a uniform magnetic field. The position of micro-actuators is fixed by photopolymerization through a photomask, followed by flipping the sample and the second UV exposure. b,c) (i) Bright-field microscopy images focusing at the top and bottom of the elastomers, respectively, showing uniaxially oriented micro-actuators at different regions. White dashed lines indicate the intersections between the adjacent regions of different height. Bright blue micro-actuators are located near the top and pale blue ones are located near the bottom of the sample in the scheme. (ii) PEGDA composite films bending upward or downward in designated regions at 180 °C (top view and side view, respectively), in comparison with (iii) FEA simulation. The blue regions in FEA indicate the domains embedded with micro-actuators on the top. Sample size: 1 cm × 0.5 cm × 200 μm. Scale bars: 100 μm.

solution by gravity, they are aligned under a uniform magnetic field, followed by application of a photomask to cure the exposed regions, where the micro-actuators are fixed in the crosslinked PEGDA. Then the sample is flipped upside down under the same magnetic field. The micro-actuators in the uncured regions migrate downward to the other side of the precursor driven by the gravitational force while maintaining the same in-plane orientation. The first stage of curing is performed for 3 s to fix the micro-actuators in the exposed regions while avoiding overcuring at the intersection between the exposed and nonexposed regions. Curing the sample preserves the alignment and height distribution of micro-actuators, which are confirmed by the bright-field optical microscopy under different focus (Figure 3b,c(i)). Accordingly, the composite film bends up or down upon heating depending on the location of the micro-actuators in the film (Figure 3b,c(ii)), as predicted by FEA simulation (Figure 3b,c(iii)).

Second, we program the in-plane arrangement of micro-actuators inside the film domain-by-domain via a series of stepwise application of the uniform magnetic field, followed by UV curing through a photomask, where the sample is rotated by 90° in-between each step (**Figure 4**a). Accordingly, we can create macroscopic director fields of the micro-actuators analogous to the "tangential +1," "radial +1," and "–1" topological defects in LCs, which are confirmed by microscopy images (Figure 4b–d(i)). Upon heating, the elastomers can bend along the designated in-plane directions to generate distinct shape change (Figure 4b–d(ii,iii)) determined by the director fields of the embedded micro-actuators, for example, forming a cone structure from the director field with "radial +1" topological defect. In the 2D film, the adjacent domains that have different director fields will restrict the actuation of each other. Thus, we cut the film along the intersections between distinct domains to release such constraints, so called kirigami, and generate more pronounced bending in each region (Figure 4b–d(iv,v)). The experimental results, both with and without cuts, agree well with the FEA simulations (Figure 4b–d(iii,v)).

While the stepwise domain-by-domain programming is successful, it is rather tedious, and the resolution of each domain is highly dependent on the resolution of the photomask and the efficiency of the photochemistry. In the third approach, we program the 2D direct field profile in a single step. We construct a 2D magnetic field by arranging four magnets, guided by COMSOL calculation, to simulate the topological defect structures (Figure S11, Supporting Information). The orientations of the micro-actuators are transverse to the magnetic field in PEGDA films. The resulting thermal actuation behaviors (**Figure 5**) are nearly identical to those seen in Figure 4 from stepwise programming and consistent with FEA. More advanced magnetic fields could be designed with arrays of multiple smaller magnets, offering faster fabrication and higher resolution of the domain size.

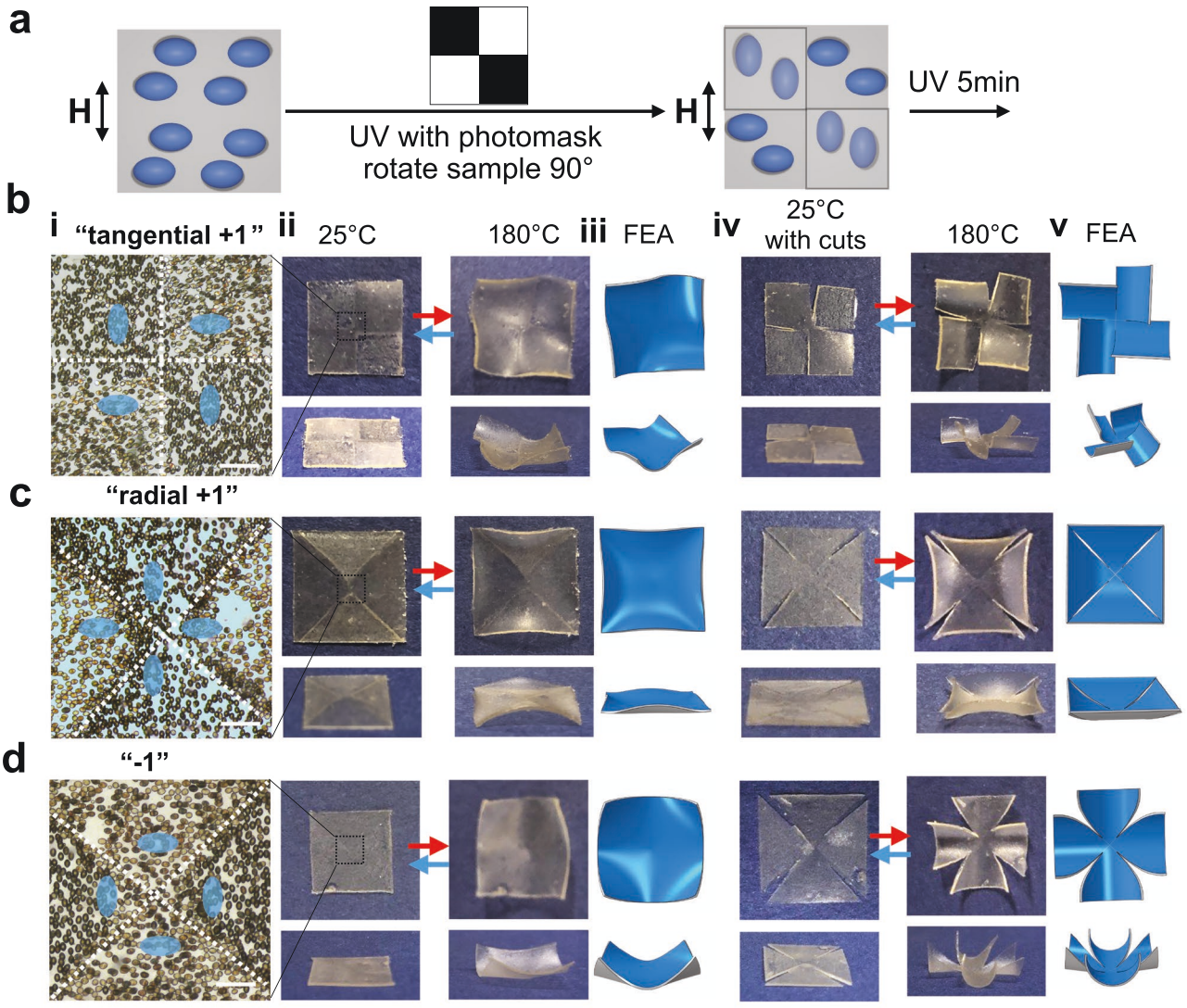

Figure 4. Bending along programmed in-plane directions by stepwise alignment and polymerization. a) Schematic illustration of controlling the 2D director field of the aligned micro-actuators inside PEGDA film through spatially selective photopolymerization using a photomask, followed by rotating sample 90° before the second photopolymerization step under a uniform magnetic field. b–d) (i) Bright-field microscopy images of the micro-actuators programmed with different orientations. (ii,iv) photographs (top view and side view) of initially flat elastomers with different regions bending along the in-plane directions on a 180 °C hot plate without (ii) and with (iv) cuts along the intersections. The cut length is 0.4 cm. (iii,v) The corresponding FEA simulations of films after bending. White dashed lines indicate the intersections between regions of different orientations of the micro-actuators. The director fields have the "tangential +1" for (b), "radial +1" for (c), and "–1" for (d) topological defects. Sample size is 1 cm × 1 cm × 200 µm. Scale bars: 200 µm.

2.4. Programming Complex Shapes

Validated by individual strategy to spatially control the in-plane orientations of the micro-actuators and their height within the film, we then combine them to demonstrate complex shape morphing. First, we perform sequential programming of the director field with "–1" defect. Different from the approach demonstrated in Figure 4, we flip the sample upside down and rotate it 90° in-plane in-between two steps of UV curing under a uniform magnetic field. While the director field of the micro-actuators are still arranged with a "–1" topological defect, they are located at different heights in the designated regions (**Figure 6**a and Figure S12a, Supporting Information). Upon heating, the elastomer bends upward initially as bending downward is inhibited by the heating surface. However, the film is now subject to competition between the in-plane and out-of-plane directions of bending, each of which is constrained within the film. When applying an external force to press the bent film, an out-of-plane "snap-through" actuation is realized together with a switch of in-plane direction of bending, which is not possible from LCEs with in-plane topological defects (Movie S2, Supporting Information). When cuts are applied,

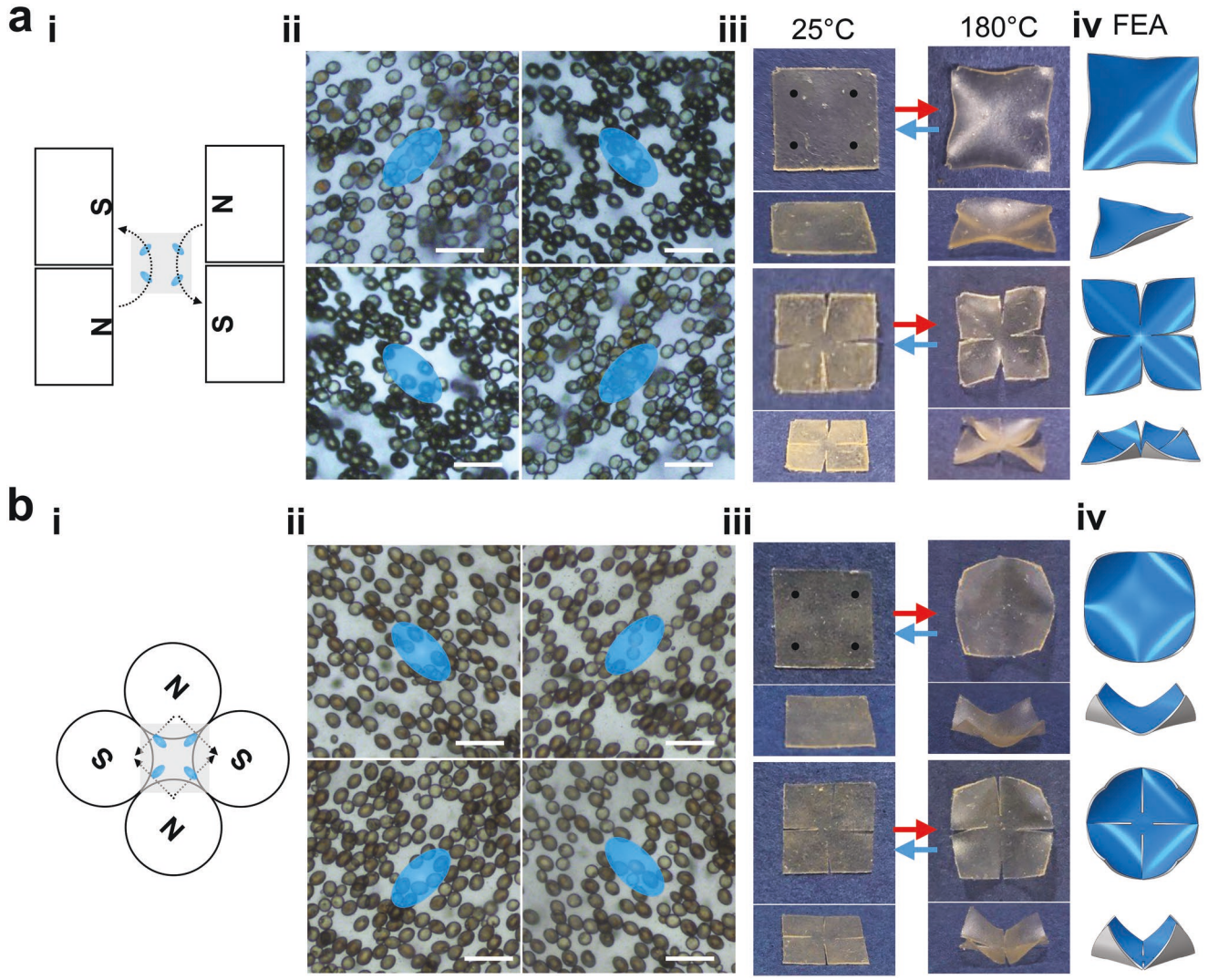

Figure 5. Bending along programmed in-plane directions using 2D magnetic fields to orient LCE micro-actuators. a,b) (i) Schematic illustration of the experimental setup. (ii) Bright-field microscopy images of the embedded micro-actuators inside the film observed at different regions of the programmed director fields. (iii) Photographs of the elastomer films without and with cuts at 25 and 180 °C. (iv) The corresponding FEA simulation of films after bending. Black dots in the photographs indicate the positions where microscopy images are taken. Director filed simulating the "–1" (a) and "radial +1" (b) topological defects in LC are directly achieved by applying designated 2D magnetic fields. Sample sizes: 1 cm × 1 cm × 200 µm with 0.4 cm cuts for (a) and 1.2 cm × 1.2 cm × 200 µm with 0.5 cm cuts for (b). Scale bars: 100 µm.

the geometrical constraints imposed by the connected regions are released so that bending of individual part is determined by the alignment direction and the height of the embedded micro-actuators (Movie S3, Supporting Information). Similarly, micro-actuators of a "radial +1" topological defect director field can be distributed at different heights to induce shape morphing from flat membrane to a negative Gaussian curvature (Figure 6b and Figure S12b, Supporting Information). Cutting the film leads to multiplex architectures where two "pedals" bent upward and the other two bent downward. The shape transformation, with or without neighboring constrains, again matches well with FEA modeling.

The 2D magnetic field can also be used in combination with flipping the sample to create director field that could be otherwise challenging to produce using a uniform magnetic field (Figure 6c). The sample with "–1" defect director field and different height distribution as shown in Figure 6c would require four steps to achieve using a uniform magnetic field, while the uniformity of the domain size is subject to the alignment of the magnet in each step. Now it only takes two steps to fabricate by applying a 2D magnetic field, producing four distinct "pedals" where each pedal bends in a distinct direction upon heating.

Last, a "crawler" with sinusoidal wave mode locomotion is made by flipping the strip after the first UV curing with a photomask of smaller feature size (0.25 mm domain size), and a quasi-2D bumpy surface is obtained from micro-actuators arranged in arrays of alternating "radial +1" and "–1" defect director fields (Figure 6d). More examples can be found in Figure S13, Supporting Information.

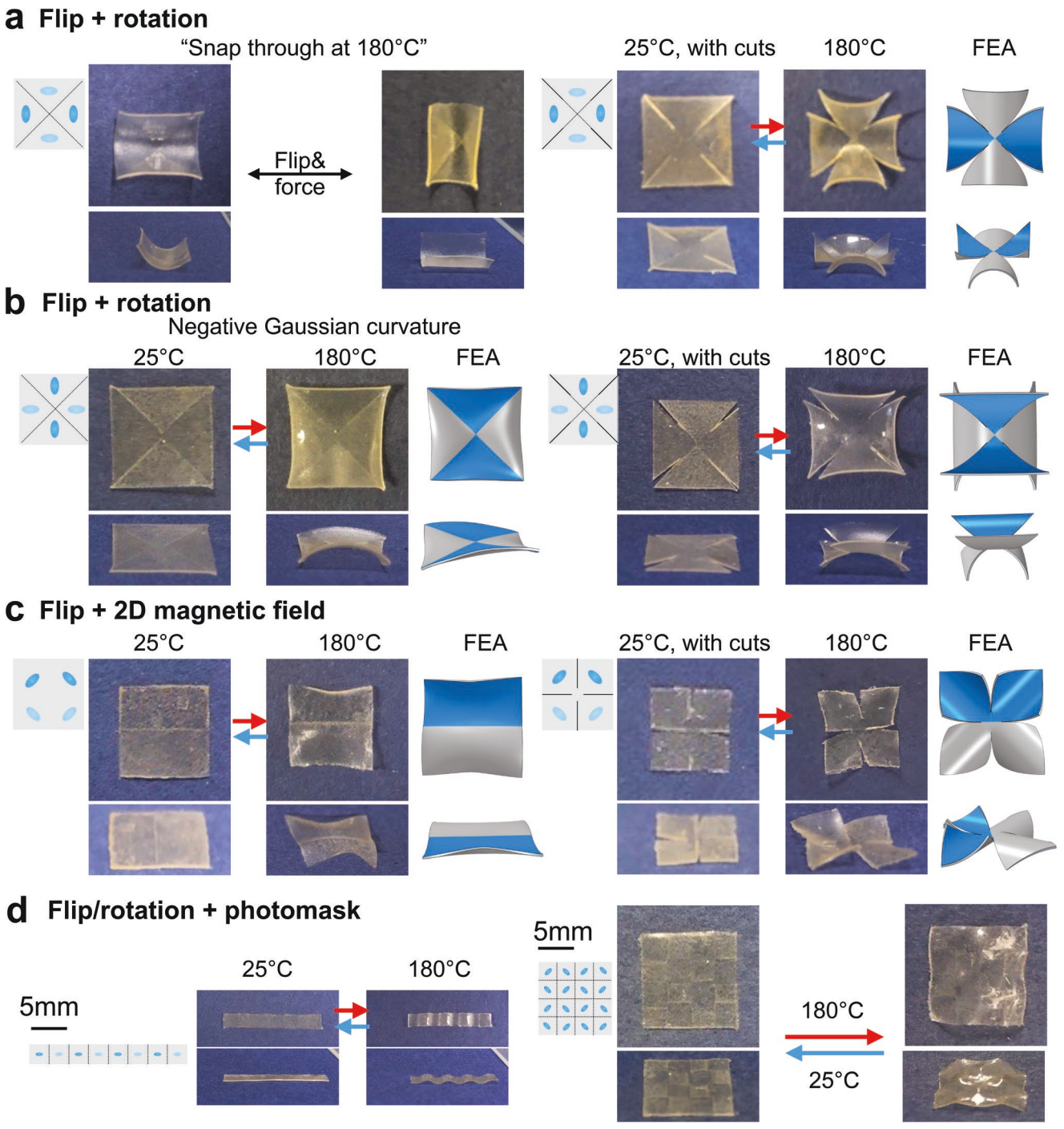

Figure 6. Complex programming and shape morphing of LCE composite films. a–d) Schematic illustration of the director field of the embedded micro-actuators (left), photographs of elastomer films at 25 and 180 °C (center), and FEA simulations of films after bending (right). a) Sample with micro-actuators arranged in the "–1" defect director field and variable height distribution undergo snap-through at 180 °C. b) Sample with micro-actuators arranged in the "radial +1" defect director field and different height distribution generates a negative Gaussian curvature at 180 °C. c) Sample with micro-actuators arranged in the "–1" defect director field and height distribution shows four distinct bending regions. d) Photomasks with smaller feature sizes lead to the fabrication of a "crawler" and a "bumpy surface." Sample sizes: 1 cm × 1 cm × 200 µm with 0.4 cm cut length for (a–c), 2 cm × 0.25 cm × 200 µm (left), and 1 cm × 1 cm × 200 µm (right) for (d).

3. Conclusion and Outlook

In summary, we synthesize dually responsive spindle-shaped LCE microparticles as "active micro-actuators" that can be spatially encoded in a conventional elastomer film to program the bending directions domain-by-domain, both in-pane and out-of-plane. The cooperative actions from the designated domains upon stimulation is consistent with the results from

FEA simulations, revealing the robustness of our approach to program actuation macroscopically in thick films (here, 200 μm). Controlling the alignment of micro-actuators is analogous to aligning the LC molecules except that it is at the micron scale. Importantly, embedding discrete micro-actuators in PEGDA films enables the separate and spatial control of complex director fields in-plane and along thickness, which is not possible to decouple when programming LCE film itself. It also allows us to broaden the material palette, where complex shapes can be realized in a conventional, isotropic elastomer with high accuracy, whereas surface anchoring requirement and the underlying substrate, and fabrication defects in LCE films would constrain the precision and degree of programmability. Here, the actuation of the building blocks (LCE micro-actuators) is rather independent of the matrix, while their spatial arrangement will determine the morphed shapes. Importantly, the actuation of the discrete micro-actuators inside the elastomer is more defect tolerant compared to LC mesogenens crosslinked in a continuous matrix as the stress induced by the shape change of a single "defect" micro-actuator can be easily dissipated to the surrounding soft network. The degree of dissipation can be tuned by adjusting the concentration of micro-actuators and the chemistry and topology of the matrix network, for example, by introducing dynamic covalent bonds for self-healing and synthesis of double networks for enhanced toughness. In comparison, any local defect in a continuous LCE network could be transmitted to nearby regions, leading to deviation from the targeted shape, especially when generating complex shapes with combined curvatures such as a face.[18] Thus, the strategy of embedding discrete micro-actuators in a soft elastomer is much more robust than programming LCE film itself. As the alignment of LC monomers is performed during the synthesis of LCE micro-actuators, the chemistry for the micro-actuators is decoupled from that for the matrix, allowing more freedom in the selection of LCEs to tune the "intelligence" of the micro-actuators. Inorganic nanoparticles with photothermal effects[52] could also be introduced to allow local actuation of the composite films by light. The arrangement of micro-actuators could be further tuned by intricate designs of photomasks and half-tone polymerization, which will find broad applications in soft robotics, smart wearables, displays, and sensors.

4. Experimental Section

Synthesis of MZF NPs: 5 mmol of Mn (II) acetylacetonate (Acros Organics), 7 mmol of zinc (II) acetylacetonate (≥98%, Acros Organics), 12 mmol of iron (III) acetylacetonate (99%, Acros Organics), 100 mmol of oleic acid (technical grade, 90%, Sigma-Aldrich), 112 mmol of oleylamine (technical grade, 70%, Sigma-Aldrich), and 72 mL of 1-octadecene (technical grade, 90%, Acros Organics) were mixed in a 250 mL flask. The reaction mixture was heated to 110 °C and kept under vacuum for 2 h. Then, the temperature was increased to 300 °C. After 2 h, the reaction mixture was cooled to the room temperature (≈ 25 °C) and MZF NPs were precipitated by adding isopropanol. The sediments were redispersed in hexane and washed further using isopropanol three times. The particles were dispersed in DCM (Fisher Scientific) with concentration of 10 mg mL^{-1} as the stock solution.

Synthesis of Oligomers: The oligomers (RM257-1,3 PDT) were synthesized following the literature.[48] In detail, 10 g 1,4-bis-[4-(3-acryloyloxy-proplyoxy)benzoyloxy]-2-methylbenzene (RM257, >95%, Wilshire Technologies Inc.) and 3.68 g 1,3 PDT (>99%, Sigma-Aldrich) were added into a 250 mL round-bottom flask. Then 100 mL DCM (Fisher Scientific) was added to dissolve these chemicals with a stirring speed at 400 rpm, yielding a transparent solution. After that, four drops (≈ 0.2 mL) of 1,8-diazabicyclo[5.4.0]undec-7-ene (Sigma-Aldrich) were added as catalyst and the solution was stirred at room temperature for 24 h. The mixture was washed with hydrochloric acid (37%, Sigma-Aldrich) aqueous solution twice (first 1 M then 0.1 M, saturated sodium chloride (NaCl, Sigma-Aldrich) was used to enhance the separation between organic phase and aqueous phase). The DCM solution was then dried by magnesium sulfate ($MgSO_4$, anhydrous powder, Fisher Scientific) for 30 min and filtrated to remove $MgSO_4$. Finally, 20 mg (0.2 wt% of RM257) butylated hydroxytoluene (BHT, Sigma-Aldrich) was added into the LC oligomer solution and the oligomers were collected as a viscous liquid after evaporating the DMC by RV 8 FLEX rotary evaporator. The viscous liquid was collected in a vial and stored in the freezer (the transparent liquid turned opaque white after 2 days in a freezer).

Fabrication of Microdroplets Using the Microfluidic Device: A flow-focusing microcapillary device was assembled for the fabrication of droplets.[53] The orifice diameter of the inner capillary was ≈ 200 μm while the outer capillary was a square capillary with 1000 μm edge length. The outer aqueous phase was 1:1 w:w glycerol (Sigma-Aldrich): 5 wt% PVA (weight-average molecular weight, Mw, 13–23k, 87–89% hydrolyzed, Sigma-Aldrich) in deionized (DI) water, and the inner organic phase was a precursors solution of 4′-pentyl-4-biphenylcarbonitrile (5CB, 272 mg, Wilshire Technologies Inc.), 1,4-bis-[4-(6-acryloyloxy-hexyloxy) benzoyloxy]-2- methylbenzene (RM 82, 100 mg, >95%, Wilshire Technologies Inc.), oligomer (RM257-1,3-PDT, 172 mg) (molar ratio of oligomer to monomer RM 82 is 1.4 to 1), MZF NPs (54 μL of 10 mg mL^{-1} in DCM), and photoinitiator 2,2-dimethoxy-2-phenylacetophenone (2 mg, Sigma-Aldrich) dissolved in DCM (2.2 mL). The aqueous phase was filtered through a PES membrane filter with 0.22 μm cut-off pore size before usage. The organic phase was filtered through a PTFE membrane filter with 0.22 μm cut-off pore size before addition of MZF NPs. 0.2 wt% MZF NPs based on the LCEs part (total weight of RM82 and RM257-1,3-PDT) was used. In experiment, flow speeds of 300 μL h^{-1} for the inner and 2400 μL h^{-1} for the outer phase were used. Droplets with diameter ≈80 μm were collected in a 20 mL vial with a solution made by mixing 5 mL 1:1 w/w glycerol: 5 wt% PVA and 5 mL water. The droplets produced in 30 min were collected in a vial.

Synthesis of the LCE Micro-Actuators: The vial with aqueous suspension of droplets was placed on a hot plate set at 50 °C with cap open overnight, with gentle shaking every a few hours to promote the evaporation of DCM and prevent particles from sticking to the bottom surface of the vial. After DCM removal, the vial was capped to prevent spilling and exposed to UV light (365 nm, 10 mW cm^{-2}) for 1 h on the 50 °C hot plate, during which the vial was gently shaken about every 10 min to prevent the particles from sedimenting to the bottom. After photopolymerization, the vial was filled with 10 mL DI water and sat still for 2 h to allow microparticles to sediment and concentrate. The supernatant (aqueous solution of water, PVA, and glycerol) was pipetted out and ethanol was added into the vial. The microparticles were suspended and redispersed in ethanol three times to extract the 5CB (over 6 h interval to ensure the full extraction), yielding LCE micro-actuators for further usage. The shape of the polymerized microparticles changed from spherical to spindle during this ethanol wash process.

Elastomer Precursors Dispersed Micro-Actuators: Elastomer precursors were prepared by mixing PEGDA (2.8 g, number-average molecular weight, Mn 700, Sigma-Aldrich), EDDT (1.08 g, 95%, Sigma-Aldrich), PETMP (0.48 g, >95%, Sigma-Aldrich), 2-hydroxy-2-methylpropiophenone (Darocur 1173, 42 mg, Sigma-Aldrich, 1.5 wt% based on PEGDA, photoinitiator), and methylhydroquinone (56 mg, Sigma-Aldrich, 2 wt% based on PEGDA, inhibitor). To embed the LCE micro-actuators into PEGDA matrix, the micro-actuators were transferred from ethanol to the elastomer precursors solution. In detail, the micro-actuators were suspended in ethanol (anhydrous, Decon

Laboratories Inc.) in a 1.8 mL centrifuge tube after synthesis. Then the suspension was left undisturbed for at least 1 h for the particles to sediment to the bottom. The supernatant (ethanol) was carefully pipetted out and 0.5 mL elastomer precursors solution was added. The tube was then vigorously shaken to suspend the micro-actuators into the elastomer precursors. This suspension was then left undisturbed for at least 2 h for the particles to sediment to the bottom. Then the supernatant (extra amount of elastomer precursors) was carefully pipetted out, leaving a designated amount of elastomer precursors. With micro-actuator made in 30 min, the volume of 125 µL precursors was left to a produce a suspension of the micro-actuators with concentration of 15% w/v (as weight in mg over the volume of the precursors in µL). Suspensions of different concentrations were made by adjusting the volume of the elastomer precursors left in the tube. The suspension should be prepared within 1 week of usage to avoid gelation.

Micro-Actuators with 1D Director Configuration in PEGDA Films: The micro-actuators suspended in PEGDA precursors in a tube were shaken to form a homogeneous suspension and deposited into the opening area of a silicone rubber spacer sandwiched by rubber-sheet-attached glass cover slides (Figure S5b, Supporting Information). The silicone rubber sheets (Ochoos) with thickness of 100, 200, 300 µm were cut into designated sizes and shapes using a Cricut Explore Air 2 Mint. The glass cover slides of 25 mm by 25 mm were purchased from Fisher Scientific and used as received. In detail, the silicone rubber sheet was attached onto a glass cover slide as the substrate, and another layer of sheet with designed opening areas was applied on top of the substrate as a spacer. After the suspension was added into the aperture of the spacer layer, another piece of rubber-sheet-attached glass cover slide was applied on top to cover and seal the opening. Then the sample was left in a uniform magnetic field set up by using two magnets (diameter 1″ thickness 0.5″, Amazing Magnets) that aligned parallel with a plastic block in between to control the distance and hold the sample (Figure S5c, Supporting Information). The sample was left undisturbed for 10 min to ensure that the micro-actuators concentrate at the bottom side before UV exposure (365 nm, 200 mW cm^{-2}) for 5 min. The sample was flipped to cure both sides to avoid crosslink gradient along the thickness. A magnetic field perpendicular to the sample plane was applied for 3 min during before UV curing to minimize the number of particles that "standing up." The sample was carefully pulled out from the rubber sheet spacer and studied.

LCE Micro-Actuators with Predefined Height or 2D Director Configurations in the PEDGA Film: The composite films with predefined out-of-plane direction of bending were made by controlling the position of micro-actuators either near the top surface or bottom surface. The elastomer precursors dispersed with micro-actuator suspension in the opening area of the spacer was prepared in the same way as described before. Then a photomask (inkjet printed on a 3M transparency film) was applied to the bottom of the sample for UV exposure (365 nm, 200 mW cm^{-2}) for 3 s from the bottom side. After the exposed region was (partially) solidified, the sample was flipped upside down and left in the same magnetic field undisturbed for 20 min. To promote particles in the uncured region to diffuse from the top side to the bottom side, the sample was put into a plastic bag (to prevent water contamination) and ultrasonication was applied in water for 1 min. Then the sample was put back to the magnetic field for another 20 min before UV exposure (365 nm, 200 mW cm^{-2}) for 5 min. Elastomer with micro-actuators with 2D "defect" patterns were made stepwise in the similar way except that the sample was rotated in the uniform magnetic field after the first UV curing of 3 s. 2D magnetic fields for creating 2D alignment in a single step were produced using multiple magnets. The position (near top or bottom side) and 2D patterns (aligning along different directions) of micro-actuators were customized by designing proper photomasks, magnetic fields, and sample flipping and rotation sequences.

Characterization: Bright-field microscopy images, videos, and polarized optical microscope images were obtained using an Olympus BX61 Motorized Microscope equipped with crossed polarizers. SEM images of microparticles were taken using an FEI Quanta 600 environmental scanning electron microscope at 3 kV electron beam. Particles were dried on a silicon substrate and sputter coated with iridium (Ir) with a thickness of 4 nm on surface before SEM imaging. The MZF NPs were characterized by JEOL F200 TEM with 200 kV electron beam. The ratio between zinc and iron was measured by inductive coupling plasma-optical emission spectrometry performed on a Spectro Genesis spectrometer with a concentric nebulizer. The direct current magnetic characterizations of magnetic NPs were carried by using a superconductive quantum interference device magnetometer with reciprocating sample option (Quantum Design MPMS-XL 7T). The hysteresis curves of magnetic NPs were measured at 300 and 15 K from 3 to −3 T. The DSC curve of micro-actuators were collected on a TA Instruments Q2000 using an aluminum hermetic crucible. Samples (5 mg of dried micro-actuators) were heated and cooled at a ramping rate of 10 °C min^{-1} for three cycles, and data from the second cycle was reported here. The photographs of elastomer samples were taken with an iPhone camera. Some images were digitally post-processed to improve brightness and contrast. The Young's modulus of the PEGDA films were calculated from the stress–strain curves obtained from the uniaxial tensile tests, which were carried out in a home-made tensile test machine (LTS300-300 mm translation stage equipped with a LSB201, 50 lb load cell). Sample size was 1 cm by 1 cm. In a typical test, the sample was fixed in two ends leaving a stretching initial distance of 5.0 mm, then the sample was uniaxially stretched at a speed of 0.2 mm s^{-1} and the force was recorded simultaneously until the sample break. The Young's modulus of the LCE micro-actuators was measured using a PeakForce QNM (Quantitative NanoMechanics) microscopy (Bruker Icon atomic force microscopy, AFM). The suspension of micro-actuators was casted onto a glass slide with a thin layer of glue to fix the micro-actuators onto the surface of the slide. Then force–displacement curves were collected using AFM on taping mode in air and then the curves were fitted to get the mechanical properties. The parameters in measuring and curve fitting were adjusted based on a standard sample with similar Young's modulus values to the micro-actuators.

FEA: The finite element method was employed to predict the shape shifting of PEGDA elastomer film with embedded micro-actuators using the commercial package ABAQUS 2020/Standard. It was assumed that the films had orthotropic expansion/shrinkage induced by the phase transition of micro-actuators and used a thermal expansion model to capture the deformation of the films. The expansion coefficients of the active layer in the principal material directions ($\alpha_{11} = -0.2$, $\alpha_{22} = 0.012$, $\alpha_{33} = 0.012$) were calculated by fitting the experimental data of the bending deformation for the samples shown in Figure 2a and Figure S9, Supporting Information. The mechanical response of the films was captured using an incompressible neo-Hookean model[54] with strain energy function W given by $W = \mu/2(I_1 - 3)$, where μ is the shear modulus of the material and I_1 is the first invariant of the right Cauchy–Green deformation tensor. Full 3D FE simulations were conducted for the sample films and the films were discretized using structured mesh of 8-node linear brick elements (ABAQUS element type: C3D8H) with mesh size of 0.04 mm to ensure that at least five elements are used to discretize the thickness of the membrane. The deformations of the films were simulated conducting nonlinear static simulations (*STATIC module in ABAQUS with NLGEOM on).

Magnetic Field Calculation: The magnetic field generated by the magnet assemblies was calculated using commercial finite element package COMSOL Multiphysics 5.4 in the magnetic field module. In the simulations, the magnetization parameter of 900 kA m^{-1} was used.

Supporting Information

Supporting Information is available from the Wiley Online Library or from the author.

Acknowledgements

The authors acknowledge support by National Science Foundation (NSF) through Materials Research Science and Engineering Center at University of Pennsylvania (DMR-1720530). S.S.Y. acknowledges partial support

from the Office of Naval Research (ONR) Multidisciplinary University Research Initiative Award N00014-18-1-2497. C.B.M. acknowledges the Richard Perry University Professorship at the University of Pennsylvania. Randall Kamien is acknowledged for helpful discussions.

Conflict of Interest

The authors declare no conflict of interest.

Author Contributions

M.L. and S.Y. conceived the ideas. M.L., S.S.Y., and Y.W. fabricated samples and collected data. L.J. performed the FEA simulations. M.L., L.J., S.S.Y., Y.W., C.B.M., and S.Y. analyzed the results. M.L. and S.Y. wrote the manuscript; and S.Y. All the authors discussed the results.

Data Availability Statement

The data that support the findings of this study are available in the supplementary material of this article.

Keywords

liquid crystalline elastomers, micro-actuators, spatial encoding, shape morphing

Received: September 19, 2022
Revised: October 24, 2022
Published online: December 20, 2022

[1] T. J. White, D. J. Broer, *Nat. Mater.* **2015**, *14*, 1087.
[2] A. Kotikian, C. Mcmahan, E. C. Davidson, J. M. Muhammad, R. D. Weeks, C. Daraio, J. A. Lewis, *Sci. Rob.* **2019**, *4*, eaax7044.
[3] R. S. Kularatne, H. Kim, J. M. Boothby, T. H. Ware, *J. Polym. Sci., Part B: Polym. Phys.* **2017**, *55*, 395.
[4] B. Zuo, M. Wang, B. P. Lin, H. Yang, *Nat. Commun.* **2019**, *10*, 4539.
[5] Q. He, Z. Wang, Y. Wang, A. Minori, M. T. Tolley, S. Cai, *Sci. Adv.* **2019**, *5*, eaax5746.
[6] C. L. Van Oosten, C. W. Bastiaansen, D. J. Broer, *Nat. Mater.* **2009**, *8*, 677.
[7] S. Li, M. M. Lerch, J. T. Waters, B. Deng, R. S. Martens, Y. Yao, D. Y. Kim, K. Bertoldi, A. Grinthal, A. C. Balazs, J. Aizenberg, *Nature* **2022**, *605*, 76.
[8] Q. G. He, Z. J. Wang, Z. Q. Song, S. Q. Cai, *Adv. Mater. Technol.* **2019**, *4*, 1800244.
[9] J. Q. Liu, Y. C. Gao, Y. J. Lee, S. Yang, *Trends Chem.* **2020**, *2*, 107.
[10] H. Kim, S. K. Ahn, D. M. Mackie, J. Kwon, S. H. Kim, C. Choi, Y. H. Moon, H. B. Lee, S. H. Ko, *Mater. Today* **2020**, *41*, 243.
[11] M. P. D. Cunha, M. G. Debije, A. Schenning, *Chem. Soc. Rev.* **2020**, *49*, 6568.
[12] Y.-Y. Xiao, Z.-C. Jiang, Y. Zhao, *Adv. Intell. Syst.* **2020**, *2*, 2000148.
[13] Y. Zhang, Z. Wang, Y. Yang, Q. Chen, X. Qian, Y. Wu, H. Liang, Y. Xu, Y. Wei, Y. Ji, *Sci. Adv.* **2020**, *6*, eaay8606.
[14] M. Pilz Da Cunha, S. Ambergen, M. G. Debije, E. Homburg, J. M. J. den Toonder, A. P. H. J. Schenning, *Adv. Sci.* **2020**, *7*, 1902842.
[15] O. M. Wani, H. Zeng, P. Wasylczyk, A. Priimagi, *Adv. Opt. Mater.* **2018**, *6*, 1700949.
[16] Y. Guo, H. Shahsavan, M. Sitti, *Adv. Mater.* **2020**, *32*, 2002753.
[17] M. Tabrizi, T. H. Ware, M. R. Shankar, *ACS Appl. Mater. Interfaces* **2019**, *11*, 28236.
[18] H. Aharoni, Y. Xia, X. Zhang, R. D. Kamien, S. Yang, *Proc. Natl Acad. Sci U. S. A.* **2018**, *115*, 7206.
[19] H. Aharoni, E. Sharon, R. Kupferman, *Phys. Rev. Lett.* **2014**, *113*, 257801.
[20] L. T. De Haan, C. Sanchez-Somolinos, C. M. Bastiaansen, A. P. Schenning, D. J. Broer, *Angew. Chem., Int. Ed.* **2012**, *51*, 12469.
[21] B. Ni, G. Liu, M. Zhang, M. Tatoulian, P. Keller, M. H. Li, *ACS Appl. Mater. Interfaces* **2021**, *13*, 54439.
[22] K. M. Herbert, H. E. Fowler, J. M. Mccracken, K. R. Schlafmann, J. A. Koch, T. J. White, *Nat. Rev. Mater.* **2022**, *7*, 23.
[23] J. Liu, Y. Gao, H. Wang, R. Poling-Skutvik, C. O. Osuji, S. Yang, *Adv. Intell. Syst.* **2020**, *2*, 1900163.
[24] A. Kotikian, R. L. Truby, J. W. Boley, T. J. White, J. A. Lewis, *Adv. Mater.* **2018**, *30*, 1706164.
[25] C. M. Yakacki, M. Saed, D. P. Nair, T. Gong, S. M. Reed, C. N. Bowman, *RSC Adv.* **2015**, *5*, 18997.
[26] Y. Wang, A. Dang, Z. Zhang, R. Yin, Y. Gao, L. Feng, S. Yang, *Adv. Mater.* **2020**, *32*, 2004270.
[27] T. H. Ware, M. E. Mcconney, J. J. Wie, V. P. Tondiglia, T. J. White, *Science* **2015**, *347*, 982.
[28] Y. Xia, G. Cedillo-Servin, R. D. Kamien, S. Yang, *Adv. Mater.* **2016**, *28*, 9637.
[29] Y. Yao, J. T. Waters, A. V. Shneidman, J. Cui, X. Wang, N. K. Mandsberg, S. Li, A. C. Balazs, J. Aizenberg, *Proc. Natl Acad. Sci. U. S. A.* **2018**, *115*, 12950.
[30] O. M. Wani, H. Zeng, A. Priimagi, *Nat. Commun.* **2017**, *8*, 15546.
[31] D. Martella, S. Nocentini, D. Nuzhdin, C. Parmeggiani, D. S. Wiersma, *Adv. Mater.* **2017**, *29*, 1704047.
[32] M. Fang, T. Liu, Y. Xu, B. Jin, N. Zheng, Y. Zhang, Q. Zhao, Z. Jia, T. Xie, *Adv. Mater.* **2021**, *33*, 2105597.
[33] Z. C. Jiang, Y. Y. Xiao, X. Tong, Y. Zhao, *Angew. Chem., Int. Ed.* **2019**, *58*, 5332.
[34] Y. Y. Xiao, Z. C. Jiang, J. B. Hou, Y. Zhao, *Nat. Commun.* **2021**, *12*, 624.
[35] J. Zhang, Y. Guo, W. Hu, M. Sitti, *Adv. Mater.* **2021**, *33*, 2100336.
[36] J. M. Boothby, T. H. Ware, *Soft Matter* **2017**, *13*, 4349.
[37] A. Resetic, J. Milavec, B. Zupancic, V. Domenici, B. Zalar, *Nat. Commun.* **2016**, *7*, 13140.
[38] S. Eristoff, S. Y. Kim, L. Sanchez-Botero, T. Buckner, O. D. Yirmibesoglu, R. Kramer-Bottiglio, *Adv. Mater.* **2022**, *34*, 2109617.
[39] X. Liu, M. Debije, H. Heuts, A. Schenning, *Chemistry* **2021**, *27*, 14168.
[40] X. Liu, X. Pan, M. G. Debije, J. P. A. Heuts, D. J. Mulder, A. Schenning, *Soft Matter* **2020**, *16*, 4908.
[41] B. Akdeniz, E. Bukusoglu, *Macromol. Rapid Commun.* **2019**, *40*, 1900160.
[42] X. Wang, E. Bukusoglu, D. S. Miller, M. A. Bedolla Pantoja, J. Xiang, O. D. Lavrentovich, N. L. Abbott, *Adv. Funct. Mater.* **2016**, *26*, 7343.
[43] L. B. Braun, T. Hessberger, R. Zentel, *J. Mater. Chem. C* **2016**, *4*, 8670.
[44] H. Yang, A. Buguin, J. M. Taulemesse, K. Kaneko, S. Mery, A. Bergeret, P. Keller, *J. Am. Chem. Soc.* **2009**, *131*, 15000.
[45] E. K. Fleischmann, H. L. Liang, N. Kapernaum, F. Giesselmann, J. Lagerwall, R. Zentel, *Nat. Commun.* **2012**, *3*, 1178.
[46] A. Buguin, M. H. Li, P. Silberzan, B. Ladoux, P. Keller, *J. Am. Chem. Soc.* **2006**, *128*, 1088.
[47] H. Yun, J. Kim, T. Paik, L. Meng, P. S. Jo, J. M. Kikkawa, C. R. Kagan, M. G. Allen, C. B. Murray, *J. Appl. Phys.* **2016**, *119*, 113901.
[48] Y. Xia, X. Zhang, S. Yang, *Angew. Chem., Int. Ed.* **2018**, *57*, 5665.
[49] H. S. Ansell, D. S. Kim, R. D. Kamien, E. Katifori, T. Lopez-Leon, *Phys. Rev. Lett.* **2019**, *123*, 157801.

[50] A. Pal, V. A. Martinez, T. H. Ito, J. Arlt, J. J. Crassous, W. C. K. Poon, P. Schurtenberger, *Sci. Adv.* **2020**, *6*, eaaw9733.
[51] K. Kim, Y. Guo, J. Bae, S. Choi, H. Y. Song, S. Park, K. Hyun, S. K. Ahn, *Small* **2021**, *17*, 2100910.
[52] Y. Wang, J. Liu, S. Yang, *Appl. Phys. Rev.* **2022**, *9*, 011301.
[53] A. S. Utada, L. Y. Chu, A. Fernandez-Nieves, D. R. Link, C. Holtze, D. A. Weitz, *MRS Bull.* **2011**, *32*, 702.
[54] R. W. Ogden, *Non-Linear Elastic Deformations*, Courier Corporation, North Chelmsford, MA **1997**.